Green Chemistry

PAPER

View Article Online
View Journal | View Issue

Cite this: *Green Chem.*, 2025, **27**, 12403

Evaluation of Ni/TiO_2 catalysts in the semi-hydrogenation of alkynols under mild conditions in water

Ajay Tomer, Laurent Djakovitch and Noémie Perret *

The semi-hydrogenation of alkynols to alkenols is an important reaction for the synthesis of fine and bulk chemicals. This work reports titania-supported nickel catalysts, prepared by wet impregnation, that demonstrate efficacy for the semi-hydrogenation of 2-methyl-3-butyn-2-ol (MBY) into 2-methyl-3-butene-2-ol (MBE) under mild conditions (30–50 °C, 10 bar H_2) in water. The impacts of titania phases, calcination temperature, and metal loading were also investigated. The anatase titania catalyst calcined at 500 °C gave the best result with 98% conversion and 80% MBE at 30 °C after 6 hours. The superior yield stems from the titania phase, MBY adsorption, metal–support interactions, and the active species' oxidation state, as evidenced using a range of characterisation and analytical techniques. These findings pave the way for the design of a stable, non-precious metal catalyst for the selective hydrogenation of alkynols under greener conditions, with the potential to supplant existing industrial methodologies.

Received 15th July 2025,
Accepted 3rd September 2025

DOI: 10.1039/d5gc03626g

rsc.li/greenchem

Green foundation

1. Our work contributes to four principles of green chemistry: the use of water as a solvent, minimized side-product formation, reactions under near-ambient conditions (30 °C), and the use of a non-precious metal (Ni). Additionally, the catalyst synthesis process is simple and does not require the use of additives or complex multi-steps.
2. Our work involved substituting a noble metal (Pd) with a non-precious metal (Ni). This approach led to significant cost savings and improved conversion (~100%) to the primary product with ~80% yield. Additionally, the catalysts showed no metal leaching.
3. Although our work does not involve the use of noble metals, high temperatures, or hazardous solvents, it does require 10 bar hydrogen pressure. A greener approach could involve performing the reactions at atmospheric pressure and with lower catalyst amounts. The use of green hydrogen could be further explored.

Introduction

The selective hydrogenation or semi-hydrogenation of alkynols to alkenols represents a fundamental process in the industrial production of numerous intermediate chemicals.[1] Alkenols, such as 2-methyl-3-buten-2-ol (MBE), are important intermediates in the synthesis of vitamins (A, E) and perfumes. For example, the synthesis of vitamin E entails a reaction between isophytol and 2,3,5-trimethylhydroquinone, with the former being derived primarily from alkenols such as linalool and MBE.[2] The synthesis of these enols is achieved *via* semi-hydrogenation of the corresponding alkynols over metal-based catalysts. Table 1 compiles the performance of previously reported state-of-the-art examples for the selective hydrogenation of MBY. This reaction is usually conducted under 10 bar of H_2, at high temperatures (80–150 °C) and in an organic solvent (ethanol, toluene, or hexane). In recent decades, noble metal-based catalysts, in particular, Pd and Pt, have been widely exploited in the semi-hydrogenation of alkynols, demonstrating excellent activity and good recyclability.[3–6] However, the selectivity usually remains low at high conversions. The selectivity issue has been circumvented through a number of routes, including the modification of Pd with p-block atoms[7] or ligands.[8] Furthermore, bimetallic catalysts (alloys or intermetallics) have also been developed to enhance alkenol selectivity by incorporating a second metal such as Pb,[9] silver, copper,[10] Bi,[11] Zn,[12–17] In[18] and Sn.[19] The introduction of a second metal has been demonstrated to modify the geometric and electronic properties of metallic Pd. This includes alterations of Pd surface species and charge transfer, which in turn weakens the adsorption of the desired enol product and improves the selectivity. The semi-hydrogenation of alkynols is a structure-sensitive reaction. Consequently, strategies such as the use of surfactants and stabilizers during the preparation of

Université Claude Bernard Lyon 1, CNRS, IRCELYON, UMR 5256, Villeurbanne, F-69100, France. E-mail: noemie.perret@ircelyon.univ-lyon1.fr

Table 1 Performances of previously reported catalysts for the selective hydrogenation of MBY

S. no.	Catalysts	Reaction conditions	Reactor	Conversion (%)	MBE yield (%)	TON	Ref.
1	$PdPb/CaCO_3$	80 °C, 10 bar H_2, ethanol	Batch	99	95	5372	18
2	Ni_2P/Ni_5P_4	30 °C, 10 bar H_2, toluene	Continuous	70	55	—	30
3	NiCu nanoalloy/MMO	30 °C, 10 bar H_2, hexane	Batch	74	52	43	31
4	Cu/SiO_2	140 °C, 10 bar H_2, toluene	Batch	100	40	12	32
5	$5Cu–Fe/Al_2O_3$	150 °C, 13 bar H_2, ethanol	Batch	100	93	15	33
6	$PdPb/CaCO_3$	30 °C, 10 bar H_2, H_2O	Batch	100	2	255	This work
7	Ni/TiO_2	30 °C, 10 bar H_2, H_2O	Batch	98	80	74	This work

Pd colloid catalysts have been reported to control the shapes of nanocrystals and enhance the enol selectivity. For instance, the use of poly(vinyl pyrrolidone) (PVP) can generate cubic, octahedral and cuboctahedral structures with diverse active sites, including facets, corners and edges, on the surface.[20,21] Despite exhibiting favorable recyclability and stability, the cost of noble metals, the necessity for additives and promoters, and the low hydrothermal stability of the catalyst represent significant limitations to their use in aqueous phase hydrogenation for industrial processes.

The replacement of noble metals such as Pd with a market value of 30 290 Euro per kg (ref. 22) with low-cost Earth-abundant metals such as nickel with a market value of 12.74 Euro per kg (ref. 23) is a promising path of research due to the abundance of nickel, its hydrogen-splitting ability, and its moderate to high activity in hydrogenation reactions.[24] The initial report on alkynol hydrogenation using RANEY® Ni has been demonstrated by Tanielyan and colleagues.[25] As reported, Ni is effective in the hydrogenation of 2-butyne-1,4-diol to 1,4-butanediol. The selectivity for alkenols was further enhanced by modifying RANEY® Ni with silica.[26] In addition, monometallic[27] and bimetallic[28,29] catalysts have been investigated with the objective of obtaining high selectivity (>90%) to 2-butene-1,4-diol. These studies collectively demonstrated that the catalytic performance was significantly influenced by the textural and acid–base properties of the supports. It is notable that only a limited number of studies have been conducted on supported Ni nanoparticles for the liquid phase hydrogenation of MBY.[30,31] In a recent study, Albani *et al.* reported the use of phosphorus-modified Ni catalysts (Ni_2P and Ni_5P_4) in the continuous flow hydrogenation of MBY, which demonstrated 70% MBY conversion and 55% MBE yield at 30 °C, 10 bar H_2, with toluene as a solvent.[30] The authors demonstrated the potential of phosphorus to create spatially isolated nickel trimers, which improved the reaction rate in comparison with unmodified nickel. In another study, Liu and colleagues demonstrated the superior activity of a bimetallic NiCu catalyst with a well-distributed homogeneous nanoalloy structure synthesized from a layered double hydroxide precursor.[31] Under the specified reaction conditions of 70 °C, 40 bar H_2 and the use of hexane as a solvent, the authors reported a 74% conversion of MBY and 52% yield of MBE within 30 minutes. Alloying Ni with Cu was found to be conducive to the creation of the "ensemble effect" and the transfer of electrons from Cu to Ni. The electron-rich Ni was beneficial for the desorption of alkene species from the catalyst. Furthermore, the catalyst exhibited excellent anti-coking.

Ni/TiO_2 has been widely used as a catalyst for aqueous phase hydrogenation reactions.[34] Indeed, titanium dioxide (TiO_2) is well known for its hydrothermal stability.[35] It has been demonstrated that the composition and morphology of the titania phase can influence the physicochemical properties of titania-supported catalysts. For example, Balaga *et al.* reported that Ni on mesoporous titania exhibits enhanced electron-rich active sites with uniform dispersion of Ni particles which resulted in ~100% furfural conversion and ~93% tetrahydrofurfuryl alcohol selectivity in water at 100 °C and under 20 bar H_2.[36] Raj and co-workers reported the catalytic activity of Ni impregnated on different titania phases for the liquid phase hydrogenation of nitrobenzene at 140 °C and 20 bar H_2 pressure. It was found that the Ni crystallite size was larger for Ni/anatase and that Ni/rutile exhibited greater metal–support interactions. The highest activity was observed for Ni/rutile catalysts with 99% conversion to aniline.[37] This knowledge can be utilized to develop efficient and stable hydrogenation catalysts with the potential to replace widely used Lindlar catalysts. To the best of our knowledge, there are no reports in the literature employing Ni/TiO_2 in the semi-hydrogenation of MBY in the aqueous phase under mild conditions.

The objective of this study was to synthesize Ni/TiO_2 by a simple wet impregnation method with the aim of tailoring the active site to achieve selective hydrogenation. Specifically, we examined the impact of calcination temperature, metal loading, and titania on both conversion and product distribution. Three TiO_2 supports were used with distinct structural and textural properties. We employed techniques such as BET, UV-Vis, XRD, H_2-TPR, MBY-TPD, XPS, and TEM to correlate the physicochemical properties with the catalytic performance evaluated in the aqueous phase MBY hydrogenation under mild conditions. This study aims to design a sustainable process for the selective hydrogenation of alkynols in water under mild conditions (30 °C) using Ni/TiO_2 catalysts as a lower-cost alternative to traditional Pd-based catalysts.

Experimental

Materials

Titania P25 (Ti-M) with mixed anatase and rutile phases was procured from Evonik. Titania with a 100% rutile phase (Ti-R)

was obtained from supplier Tronox. A high-surface-area titania with 100% anatase phase (Ti-A) was procured from Sachtleben Chemie GmbH. Nickel nitrate hexahydrate ($Ni(NO_3)_2{\cdot}6H_2O$, >99 wt%), supplied by Sigma-Aldrich, was used as a precursor for Ni impregnation. Isopropyl alcohol (IPA, HPLC grade >99.99%) was used as an internal standard. The reactant 2-methyl-3-butyn-2-ol (MBY) and the products 2-methyl-3-butene-2-ol (MBE) and 2-methyl-butan-2-ol (MBA) were supplied by Sigma-Adrich. All the reagents were used without further purification.

Catalyst preparation

A series of nickel catalysts was synthesized *via* a wet impregnation process, utilizing an aqueous solution of nickel nitrate salt and a titania support. Briefly, a solution of varying concentrations of Ni(II) nitrate hexahydrate was added to 60 mL of distilled water. Subsequently, the solution was stirred for five minutes, after which 5 g of support was added. The mixture was then subjected to stirring for two hours at room temperature. Subsequently, the water was removed at 60 °C until the system reached a dry state, utilizing a rotary evaporator. The solid was dried overnight at 80 °C and then calcined under air flow (100 ml min^{-1}) at 300, 400, and 500 °C for 2 h using a heating ramp of 3 °C min^{-1}. The calcined catalyst was then reduced at 500 °C for 2 h under a hydrogen flow of 100 ml min^{-1}. Following this, the catalyst was passivated for a period of three hours under 1% O_2–N_2 (60 ml min^{-1}). The synthesized Ni-based catalysts were prepared with the Ti-M, Ti-A, and Ti-R supports and were designated as *x*Ni/Ti-M_T, *x*Ni/Ti-A_T, and *x*Ni/Ti-R_T, respectively, where *x* represents 5 or 10 wt% Ni loading, M, A and R represent mixed, anatase and rutile phases of titania, and T denotes the calcination temperature.

Catalyst characterization

The bulk metal composition of the calcined catalysts was determined by means of an Agilent-5800 inductively coupled plasma-optical emission spectrometry (ICP-OES) apparatus. Prior to analysis, the samples were subjected to digestion in a mixture of H_2SO_4, HNO_3 and HF at 110 °C.

The Brunauer–Emmett–Teller surface areas (S_{BET}), total pore volume (PV) and mean pore diameter (PD) of the various samples were measured from the N_2 adsorption/desorption isotherms using a Micromeritics ASAP 2020 instrument. Prior to the measurements, the samples were degassed at 150 °C for a period of three hours. The surface areas were calculated in the relative pressure range of $0.05 < P/P_0 < 0.25$, while the pore volume was measured at $P/P_0 = 0.99$.

X-ray diffraction (XRD) patterns were recorded in the range of 2θ = 10–80° at a rate of 0.04° s^{-1}, using a Bruker D8A25 X-ray diffractometer equipped with a Cu Kα radiation source (λ = 1.5418 Å) and a Lynxeye detector. The Scherrer equation was employed to ascertain crystallite sizes. The phase composition of titania was calculated from the most dominant crystallographic planes (101) and (110) of anatase and rutile, respectively, using the equation Anatase % = 100/{1 + 1.265(Ir/Ia)}, where Ia and Ir are the peak intensities of anatase and rutile, respectively.[38] The average crystallite sizes of anatase (d_A) and rutile (d_R) titania were estimated by applying the Scherrer equation to the (101) and (110) planes, while the (200) plane was used for nickel (d_{Ni}) and nickel oxide (d_{NiO}).

The diffuse-reflectance UV-Vis (DRUV-Vis) spectra of the calcined catalysts were recorded in diffuse reflectance mode on a Lambda 1050+ PerkinElmer Microspectrophotometer equipped with an integrating sphere with a 100 mm diameter. The standard used was $BaSO_4$.

The temperature-programmed reduction (H_2-TPR) profiles were obtained using a Micromeritics AutoChem III 2930 instrument, which was equipped with an auto-generated cold trap and a thermal conductivity detector (TCD). The reduction profiles were recorded by reducing the calcined catalysts (100 mg) under 10%H_2–Ar flow (50 ml min^{-1}) in the temperature range of 30–700 °C using a heating rate of 10 °C min^{-1}. The percent reduction was calculated by dividing the experimental hydrogen consumption value by the theoretical one. To estimate the reduction activation energy, heating rates of 5 and 15 °C min^{-1} were also employed.

Temperature-programmed desorption (TPD) of NH_3 was conducted on the same apparatus. Briefly, the calcined samples (100 mg) were first reduced under hydrogen up to 500 °C. After cooling to 100 °C, the samples were saturated with NH_3 in a series of pulses, after which a helium atmosphere was employed for purging until the stable baseline was achieved. This process was undertaken in order to remove any physisorbed gases. Subsequently, the samples were heated from 50 to 700 °C at a rate of 10 °C min^{-1} under a flow of helium. The amount of NH_3 released was quantified using a TCD.

Vapor flow-TPD of MBY was performed on a Micromeritics AutoChem III 2930, which was equipped with a vapor generator flask. Shortly, 40 mL of reactant was kept in a 100 ml conical flask and heated at 105 °C to facilitate vapor deposition on the reduced catalyst. Around 100 mg of catalyst was reduced at 500 °C for 30 minutes. After cooling to 40 °C (similar to the reaction temperature), the catalyst was saturated with MBY vapours for 30 minutes under a helium flow rate of 30 ml min^{-1}. Then, the sample was purged under a helium stream for 1 h. Finally, the samples were heated from 40 to 700 °C at a heating rate of 10 °C min^{-1}. The amount of MBY desorbed was quantified by TCD.

The surface chemical composition and chemical states of Ni were analysed by X-ray photoelectron spectroscopy (XPS) using a Thermo Scientific Nexsa G2 instrument with an Al monochromatic (1486.6 eV) X-ray source. The binding energies were referenced to the C_{1s} peak set at 284.5 eV. The samples were deposited on an indium support. Quantitative analysis was performed by peak decomposition and fitting using Casa XPS and Igor Pro software.

A transmission electron microscope (TEM) was employed to characterize the morphology and local composition of the various catalysts. The analysis was conducted with a TEM FEG JEOL 2100F equipped with EDS. Prior to analysis, the samples were directly dispersed on carbon-coated copper grids.

Catalytic tests in semi-hydrogenation

The semi-hydrogenation of MBY was performed in a 300 ml Parr 4566 series mini bench-top reactor with a 4843-control system. In a typical reaction, 1 g of MBY was combined with 40 ml of H_2O and 0.1 g of a reduced catalyst in an autoclave. Subsequently, the reactor was sealed and flushed three times with argon, followed by flushing with H_2. The autoclave was pressurized with 10 bar of H_2, heated at varying temperatures (30 and 50 °C) and stirred at 900 RPM for a variable reaction time (2, 4, 6 h). To ensure the accurate monitoring of the reaction progress, the reaction mixture was collected at a specific time interval. Prior to GC analysis, the samples were filtered using a 0.45 μm nylon syringe filter. The reactant (MBY) and products (MBE and MBA) were analysed using an Agilent 6890 GC equipped with an FID detector and a polar capillary column (VARIAN VF WAX, 30 m × 250 μm × 0.25 mm) with isopropyl alcohol (IPA) as an internal standard. The MBY conversion, the yield to the products, mass balance and turnover number (TON) were defined as follows:

$$\text{Conversion}\,\% = \left(1 - \frac{n[\text{MBY}]_t}{n[\text{MBY}]_0}\right) \times 100$$

$$\text{Yield}\,\% = \frac{n[\text{MBE}]_t}{n[\text{MBY}]_0} \times 100$$

$$\text{Mass balance}\,\% = (n[\text{MBY}]_t + n[\text{MBE}]_t + n[\text{MBA}]_t)/n[\text{MBY}]_0 \times 100$$

$$\text{TON} = \frac{n[\text{MBY}]_0}{n_{\text{Ni}}} \times \frac{\text{Conversion}}{100}$$

where $n[\text{MBY}]_0$ and $n[\text{MBY}]_t$ represent the initial and final moles of the reactant MBY, respectively. Meanwhile, $n[\text{MBE/MBA}]_t$ denotes the moles of the product MBE or MBA formed at the specified reaction time t. The TON was calculated by dividing the number of moles of MBY converted per mole of nickel used in the reaction.

Catalyst recycling

The stability of the catalysts was assessed through the implementation of repeated runs. In a typical experiment, following the completion of the initial reaction run, the catalyst was separated from the reaction mixture by centrifugation and underwent two washes with 40 mL of distilled water. The catalyst was subjected to an overnight drying process at 80 °C and subsequently calcined under air at 500 °C for 2 h. Thereafter, the catalyst was reduced under a hydrogen flow at 500 °C for a further 2 h, followed by a passivation process under 1% O_2–N_2 for 3 h before the next run. Two reusability tests were conducted to demonstrate the robustness of the synthesized catalysts. Additionally, spent calcined catalysts were also subjected to ICP analysis to ascertain the extent of metal leaching. TGA was performed on a dried spent catalyst.

Results and discussion

Characterization of catalysts

A series of Ni catalysts supported on TiO_2 was synthesized by means of wet impregnation, employing three different titania supports: mixed titania (Ti-M), anatase titania (Ti-A), and rutile titania (Ti-R). The synthesis process entailed the impregnation of the titanium oxide supports with nickel loadings of 5 and 10 wt%. The supports were subsequently calcined at three distinct temperatures: 300, 400, and 500 °C and reduced at 500 °C before the hydrogenation reaction.

Textural analysis

Fig. 1 depicts the nitrogen adsorption–desorption isotherms of 10%Ni supported on the different titania supports and calcined at 500 °C. The isotherm of the supports is shown in Fig. S1. Table 2 provides a summary of the physicochemical properties of the synthesized catalysts. The parent titania (Ti-M, Ti-A and Ti-R) and their respective nickel-doped catalysts exhibit type IV isotherms, which are characteristic of mesoporous materials. However, they differ in the formation of the hysteresis loop. For instance, 10Ni/Ti-M_500 and 10Ni/Ti-R_500 catalysts show an H1 hysteresis loop, exhibiting two parallel and nearly vertical adsorption and desorption branches over a considerable range of gas pressure. An H1 hysteresis loop is typically observed in materials with a uniform cylindrical or spherical pore shape. In contrast, the titania Ti-A-based catalyst (10Ni/Ti-A_500) exhibits an H3 type hysteresis loop, which is indicative of materials comprising platelet particles that form slit-shaped pores. The decrease in specific surface area after the loading of nickel suggests that the titania surface is partially covered by these particles while retaining the original structure. Only the 10Ni/Ti-A_500 catalyst exhibited a narrow pore size distribution, with an average pore diameter of 15 nm. In comparison, both the 10Ni/Ti-M_500 and 10Ni/Ti-

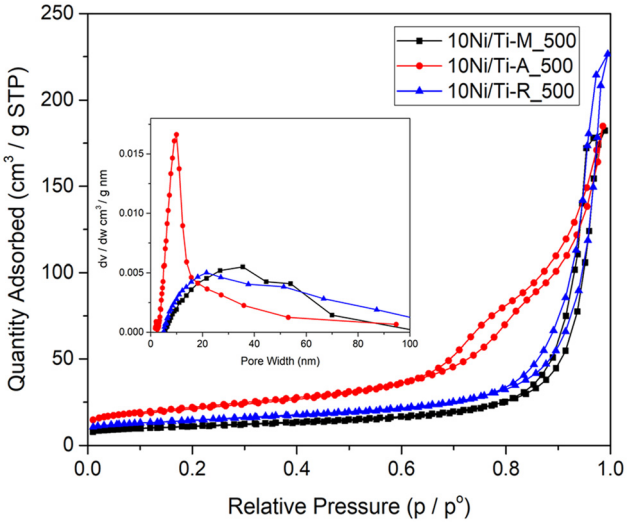

Fig. 1 N_2 adsorption–desorption isotherms (inset: pore size distribution) of nickel-supported catalysts prepared by wet impregnation.

Table 2 Physico-chemical properties of Ni catalysts

S. no.	Catalyst	Ni[a] (wt%)	S_{BET}[b] (m^2 g^{-1})	d_{Ni}[c] (nm)	%Red.[d]	Strength of acidic sites[e]			
						Weak (%)	Medium (%)	Strong (%)	Total (μmol g^{-1})
1	10Ni/Ti-M_300	9.9	44	14	101	54	46	—	142
2	10Ni/Ti-M_400	9.9	42	15	95	65	35	—	133
3	10Ni/Ti-M_500	9.5	40	24	101	41	59	—	145
4	5Ni/Ti-M_500	5.1	49	16	91	66	30	4	151
5	10Ni/Ti-A_300	10.1	186	11	99	55	45	—	253
6	10Ni/Ti-A_400	9.8	171	11	92	51	49	—	234
7	10Ni/Ti-A_500	9.3	78	11	89	42	54	5	211
8	5Ni/Ti-A_500	5.2	107	12	90	49	48	3	221
9	10Ni/Ti-R_300	10.3	66	9	75	40	60	—	144
10	10Ni/Ti-R_400	10.4	59	11	76	56	44	—	117
11	10Ni/Ti-R _500	11.1	51	12	87	33	63	4	201
12	5Ni/Ti-R_500	5.4	50	—	74	36	64	—	192

[a] Measured by ICP-OES. [b] BET surface area. [c] Average crystallite size of Ni calculated using the Scherrer equation. [d] Obtained from H_2-TPR analysis. [e] Obtained from NH_3-TPD analysis.

R_500 catalysts demonstrated a wide range of pore size distributions, with average diameters of 31 and 33 nm, respectively.

As illustrated in Fig. S1, the isothermal plots reveal a notable alteration in surface area, pore volume and pore size when the catalysts undergo calcination at temperatures ranging from 300 to 500 °C. In comparison with Ti-M and Ti-R, this effect is more pronounced in Ti-A based catalysts, where the surface area decreased from 186 m^2 g^{-1} for the catalyst calcined at 300 °C (10Ni/Ti-A_300) to 78 m^2 g^{-1} for the catalyst calcined at 500 °C (10Ni/Ti-A_500). This reduction in surface area is typically ascribed to the process of particle agglomeration.[39] Similarly, the average pore size increased from 6.2 to 15.6 nm. The lower nickel-based catalysts (5 wt%) show similar isothermal profiles with minimal alteration in surface area (Fig. S2).

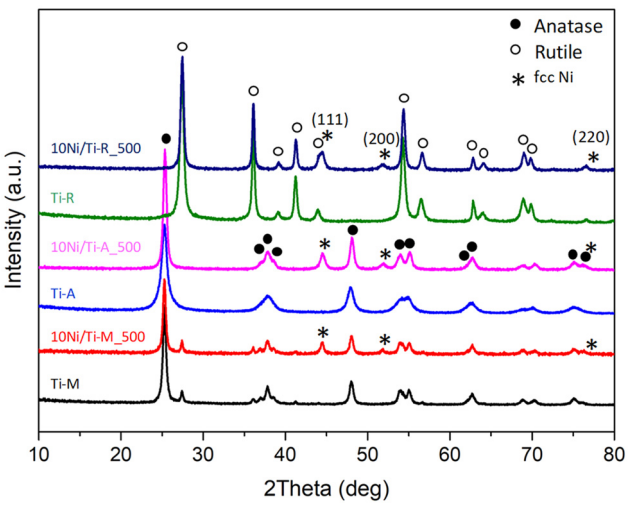

Fig. 2 XRD patterns of reduced Ni catalysts along with their parent titania.

X-Ray diffraction

X-ray diffraction patterns of the bare titania (Ti-M, Ti-A and Ti-R) exhibiting diverse compositions are presented in Fig. 2. Based on ICDD files, the characteristic peaks of the crystal phases of titania, namely anatase (PDF# 01-084-1285) and rutile (PDF# 01-084-1283) can be discerned. It should be noted that for the Ti-R, only the peaks corresponding to the rutile phase were detected. Similarly, Ti-A exhibited exclusively the anatase phase. The rutile content in the mixed phase titania was determined to be 13%. The crystallite sizes of the supports (Table S1) are smaller for Ti-A (d_A = 7 nm) and Ti-R (d_R = 11 nm) than for Ti-M (d_A = 14 nm; d_R = 25 nm).

The impact of calcination temperatures (300, 400 and 500 °C) was investigated to gain insight into the crystal growth of the titania phase and nickel oxide in Ti-M, Ti-A, and Ti-R catalysts. The XRD diffractograms of the solids after impregnation and calcination are included in Fig. S3(a, c and e). No change in the crystallite size of titania and the anatase (85–86%) and rutile (14–15%) phase content was observed with increasing calcination temperature (Table S1, entries 2–4). The characteristic reflections of NiO (PDF# 00-047-1049) were observed at 2θ = 37.2°, 43.3° and 62.8°, corresponding to (111), (200) and (220) indices, respectively. It is noteworthy that in the case of Ni/Ti-M, the NiO (200) peak can be visualized even at a low calcination temperature (300 °C) and the peak further intensifies with increasing calcination temperature. This indicates aggregation on the surface.[40] The NiO crystallite size was found to increase with temperature, from 15 to 21 nm (Table S1, entries 2–4).

In contrast, no diffraction peak corresponding to NiO (200) at 2θ = 43.3° could be detected in Ti-A catalysts calcined at 300 and 400 °C, indicating the presence of well-dispersed NiO on the surface of TiO_2. Upon increasing the calcination temperature to 500 °C, a broad NiO (200) peak with a crystallite size of 6 nm was observed along with an increase of the anatase phase from 7 to 9 nm (Table S1, entries 10–12). To facilitate comprehension of the decomposition of nitrate salt to nickel oxide on the three titania, thermogravimetric analysis of the

catalysts after impregnation and drying was also performed. As seen from Fig. S4, the decomposition of the Ni precursor on mixed M and rutile R titania occurs in the temperature range of 150–250 °C, while it takes place at higher temperatures on the anatase A titania catalyst (from 200 to 380 °C). These results show that the decomposition of nickel salt to NiO is delayed on the anatase support.

The solids were then reduced at 500 °C. The X-ray diffraction patterns of 10Ni/Ti_500 catalysts are presented in Fig. 2 as representative examples, while 10Ni/Ti_300 and 10Ni/Ti_400 are included in Fig. S3. No peaks corresponding to Ni_2O_3 and $NiTiO_3$ are observed and the absence of NiO peaks ensures complete reduction of NiO to Ni. The characteristic peaks of the face-centered cubic structure of nickel (PDF# 00-004-0850) were observed at 2θ = 44.5°, 51.8° and 76.4°, corresponding to (111), (200) and (220) planes, respectively. As a result of the overlap of the peak associated with Ni (111) at 2θ = 44.5° with a peak of the rutile phase at 2θ = 43.9°, the average Ni crystallite size (d_{Ni}) was calculated with the peak at 2θ = 51.8° of Ni (200).

The mean crystallite sizes of Ni in Ti-M, Ti-A and Ti-R calcined and reduced at 500 °C were determined to be 24, 11 and 12 nm, respectively. The same trends were observed after reduction as seen after calcination. Indeed, the average nickel crystallite size was observed to increase a lot for 10Ni/Ti-M catalysts (from 14 to 24 nm, Table 2, entries 1–3). In contrast, the average nickel crystallite sizes remain close in 10Ni/Ti-A (~11 nm, Table 2, entries 5–7) and 10Ni/Ti-R catalysts (9–12 nm, Table 2, entries 9–11), indicating that these supports must stabilize NiO growth during the thermal treatment. Moreover, the incorporation of Ni in Ti-M titania results in a small transformation of the anatase phase towards the rutile phase, from 87 to 83%, as the temperature increased from 300 to 500 °C. This change is attributed to the ability of nickel to lower the phase transformation energy.[41] In opposition to this, the anatase phase in the 10Ni/Ti-A catalysts remained stable. The results demonstrate that the nature of the support and the calcination temperature have a strong impact on the growth of the NiO phase, hence the Ni phase, which might be due to different metal–support interactions.

UV-visible by diffuse reflectance spectroscopy

The application of UV-Vis analysis facilitated the acquisition of valuable insights pertaining to the charge transfers and d–d transitions. The UV-Vis spectra of the 10Ni/Ti-M_500, 10Ni/Ti-A_500, and 10Ni/Ti-R_500 catalysts, in addition to the Ti-M support, are presented in Fig. 3. The parent titania Ti-M exhibits two shoulders around 225–280 nm and 280–350 nm, which are characteristic of $O^{2-} \rightarrow Ti^{4+}$ charge transfer.[42] These peaks may undergo alteration with the incorporation of metal ions. Moreover, Ti-M exhibits an absorption band edge in the ultraviolet region at approximately 370 nm. It is noteworthy that all nickel-based catalysts exhibit a red shift with the absorption edge falling in the visible region (400–550 nm). The absorption band in this region is attributed to charge transfer from O 2p to the Ni d-states.[43] The 10Ni/Ti-A_500 catalyst exhibits the highest charge transfer with the maximum shift to the higher wavelength. The phenomenon of charge transfer in the catalyst is of significant importance, as it has the potential to render metal–hydrogen species more nucleophilic, thereby enhancing their reactivity towards alkynes in comparison with alkenes. The broad bands in the higher region (600–800 nm) represent d–d transitions of Ni orbitals and could indicate the presence of surface defects and oxygen vacancies. These findings are supported by previous studies.[41,44,45] Notably, the intensity and appearance of this band vary in the three titania samples, with titania Ti-R exhibiting a more pronounced effect. This suggests a stronger interaction between NiO and TiO_2. The finding aligns with the reduction profiles presented *vide infra*.

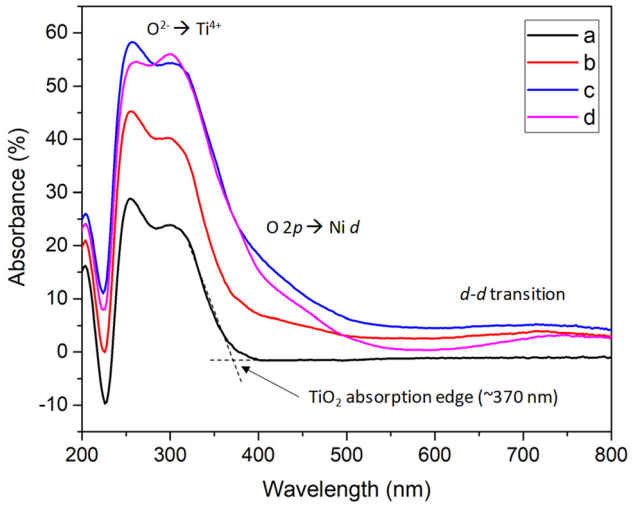

Fig. 3 DRUV-Vis profiles of the calcined nickel catalyst on different titania: (a) Ti-M, (b) 10Ni/Ti-M_500, (c) 10Ni/Ti-A_500 and (d) 10Ni/Ti-R_500.

Catalyst reducibility

The H_2-TPR experiment was carried out to investigate the reducibility of the calcined samples and the interaction between nickel species and the support. Fig. 4(a–c) depicts the reduction profile of the Ti-M, Ti-A, and Ti-R supported catalysts calcined at different temperatures, while Table 2 and Table S2 provide a summary of the experimental hydrogen consumption values, reduction temperatures, and percent reduction.

When looking at all the profiles, the catalysts exhibit distinct reduction behaviour which depends strongly on the support and calcination temperature (particularly at 300 °C). Two kinds of peaks are observed: low-temperature peaks corresponding to the weakly bound NiO on the support and high-temperature peaks indicating strong interactions of NiO with TiO_2. For instance, the 10Ni/Ti-M_300 catalyst exhibits three reduction peaks, situated at 204, 310 and 381 °C, which are attributed to the nickel oxide species of varying dimensions interacting with the surface titania. The single peak at

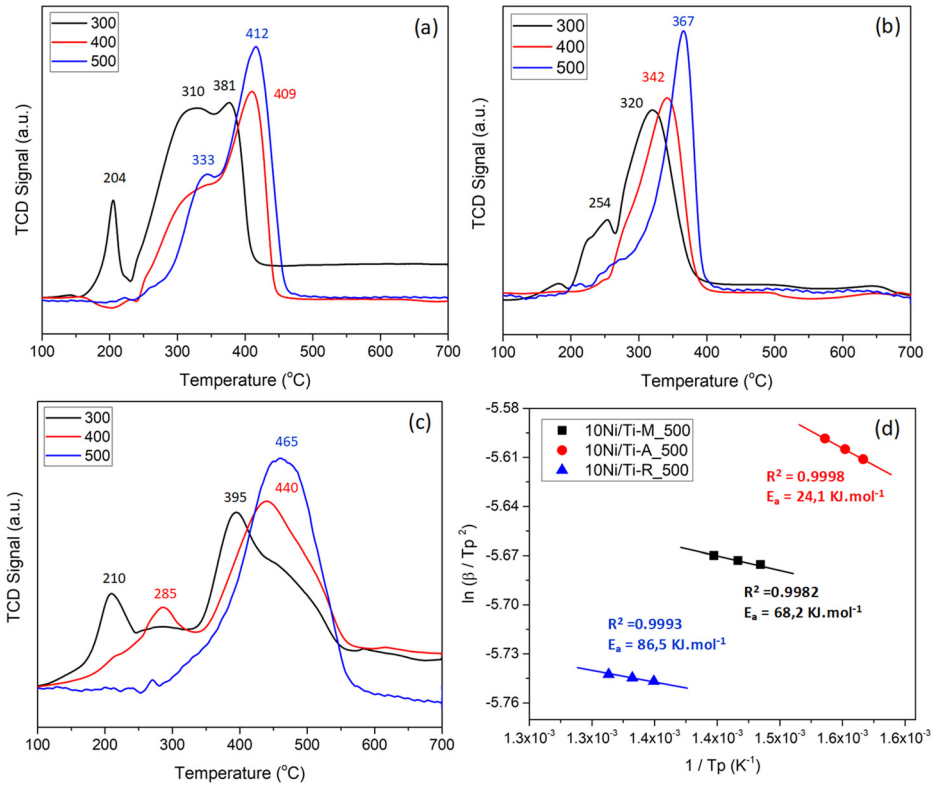

Fig. 4 H_2-TPR profiles of (a) 10Ni/Ti-M, (b) 10Ni/Ti-A, and (c) 10Ni/Ti-R catalysts calcined at 300, 400 and 500 °C and (d) Kissinger plot of the three 10%Ni–titania catalysts.

204 °C represents the weakly bound NiO species with minimal interactions on Ti-M titania, while those at 310 and 381 °C temperature attributed to moderate to strongly bound NiO species on the titania surface. As the calcination temperature was increased to 400 °C (10Ni/Ti-M_400), the reduction pattern underwent a transformation, manifesting as two distinct peaks: a shoulder peak around 300 °C and a main peak centered at 409 °C. Further increasing the calcination temperature to 500 °C results in a shift of the main peak to 412 °C with a concomitant decrease in the concentrations of weakly bound NiO species. As indicated in Table S2 and Table 2, the consumption of hydrogen is nearly complete with regard to the reduction of the NiO species. In the case of Ti-R-based catalysts, a broad reduction peak is observed, spanning from 300 to 580 °C. This peak is attributed to the reduction of highly interacting NiO on TiO_2 and may also be indicative of a partial reduction of Ti^{4+} to Ti^{3+}.[46] The 10Ni/Ti-R_300 catalyst exhibits two reduction peaks: a smaller peak at 210 °C and a broader peak centered at 395 °C. These peaks are attributed to weak and strong NiO interaction with rutile titania. Increasing the calcination temperature from 300 to 500 °C results in a shift of the reduction peak from 395 to 465 °C, indicating a stronger interaction of nickel oxide with the support. This observation is corroborated by decreases in the percent reduction values of NiO, which range from 75% to 87% (Table 2, entries 9–11). In contrast to the Ti-M and Ti-R catalysts, the Ti-A-based catalysts exhibit different reduction profiles. At a low calcination temperature, the 10Ni/Ti-A_300 catalyst exhibits only two peaks: a minor peak at 254 °C and a principal intense peak at 320 °C. This demonstrates the existence of a smaller quantity of weakly bonded NiO species in comparison with the 10Ni/Ti-M_300 catalyst. Further increases in the calcination temperature result in a reduction in the number of weakly bound species, leaving only those that interact strongly with the surface. This is corroborated by the observation of a single reduction peak at 342 °C and 367 °C, respectively. This suggests that NiO particles exhibit a homogeneous size distribution.

The effect of nickel loading was also investigated (Fig. S6, Table 2, and Table S2). The nickel content exerts a small influence on the reduction behaviour, evident in the form of peak shape, intensity, and shift of the reduction temperature. The main difference concerns 5Ni/Ti-M_500, which exhibits a single reduction peak centred at 401 °C instead of the two peaks observed in 10Ni/Ti-M_500. Moreover, the percent reduction values were found to be slightly lower in 5Ni/Ti-R_500 and 5Ni-T-A_500 catalysts (Table 2 entries 4 and 12).

The observed trends in metal–support interactions are in accordance with the findings reported in the literature.[43] Moreover, it has been demonstrated that supported catalysts with larger Ni particles exhibit a reduction in metal–support interactions, whereas smaller particles result in an enhance-

ment of metal–support interactions.[47] Irrespective of calcination temperature, the maximum reduction temperature follows the order: Ni/Ti-R > Ni/Ti-M > Ni/Ti-A. The rutile-based catalysts exhibit a greater degree of NiO interaction in comparison with the anatase and mixed-phase-based catalysts. It is worth noting that the pure anatase support Ti-A facilitates the NiO reduction compared to Ti-M (87% anatase + 13% rutile) and Ti-R (100% rutile), in agreement with the literature.[46] It can be observed that the calcination temperature exerts an influence on the distribution and interaction of NiO species, as well as on the reduction of nickel oxide. Finally, the maximum reduction temperature of 500 °C used to reduce the catalysts before the hydrogenation reaction ensures the complete reduction of oxide species to active Ni species.

To further illustrate the effect of the titania phases on the reduction rate, the apparent reduction activation energy (E_a) of the calcined catalysts (calcined at 500 °C) was obtained using the Kissinger equation,[48] as expressed by eqn (1).

$$\ln\left(\frac{\beta}{T_p{}^2}\right) = -\frac{E_a}{RT_p} + B \quad (1)$$

where β is the linear heating rate (in K s^{-1}), T_p is the absolute temperature corresponding to the position of the maximum reduction peak that can be measured from the experimental H_2-TPR profiles of the corresponding oxides at varying heating rates (β) (Fig. S5), R is the universal gas constant (8.314×10^3 kJ mol^{-1} K^{-1}), E_a is the reduction activation energy (in kJ mol^{-1}), and B represents a constant associated with the Kissinger equation. By employing this equation, one can generate a plot with a linear trend and a slope equal to $-E_a/R$, as shown in Fig. 4d. As can be seen in the plot, the data points fall on straight lines with correlation coefficients (R^2) of ≥0.998. As evidenced by the plot, the activation energy follows the order: Ni/Ti-R (86.5 kJ mol^{-1}) > Ni/Ti-M (68.2 kJ mol^{-1}) > Ni/Ti-A (24.1 kJ mol^{-1}). These results indicate that the release of oxygen from NiO to form metallic Ni is a relatively facile process for the 10Ni/Ti-A_500 catalyst. The calculated reduction activation energies for Ti-M and Ti-R are consistent with previously reported values.[49,50] The E_a value associated with Ti-A is relatively low, which may be attributed to the small NiO particle size and low metal–support interactions.[51] As particle size decreases, the number of surface atoms increases, necessitating less energy for reduction. As the metal–support interaction is low, the removal of oxygen close to the support is also easier. These results collectively demonstrate the pivotal role of titania phases in the reducibility of NiO species.

Estimation of surface acid sites by NH_3-TPD

It is well documented in the literature that the titania surface exhibits both acidic and basic sites, which are subjected to modification by thermal treatment processes. The co-ordinately unsaturated surface metal ions are responsible for the acidic sites, while surface anions or anion vacancies contribute to the basic sites.[52] In this regard, the qualitative and quantitative numbers of acidic sites were determined by NH_3-TPD. Table 2 lists the percent strength of weak, moderate and strong acidic sites and total acid sites on the reduced catalysts, while Fig. 5 represents the NH_3-TPD profiles of 10Ni/Ti-M, 10Ni/Ti-A, and 10Ni/Ti-R catalysts calcined at different temperatures.

The peaks were assigned to three ranges of acidic sites based on their temperature: weak acidic sites were observed at temperatures between 100 and 250 °C, medium acidic sites at temperatures between 250 and 400 °C, and strong acidic sites at temperatures above 400 °C. For all the catalysts, the primary contribution to the total acidity comes from weak and medium acid sites and their percent contributions lie in a similar range (~50%). An analysis of the three titania samples calcined at 500 °C revealed that the number of acid sites increases following the order 10Ni/Ti-M < 10Ni/Ti-R < 10Ni/Ti-A. A similar trend in the acidic strengths has been reported in the literature, with anatase exhibiting higher total acidity than rutile, which was attributed to the higher surface area.[34]

From Fig. 5, it is evident that elevated calcination temperatures exert a considerable influence on the acidic sites, particularly in 10Ni/Ti-A catalysts (Fig. 5b). Noteworthily, in the case of 10Ni/Ti-M, the catalyst calcined at 300 °C (10Ni/Ti-M_300) exhibits an intense peak at 210 °C, accompanied by two additional peaks at 298 °C and 364 °C, which are attributed to weak and medium acid sites, respectively (Fig. 5a). However, an increase in the calcination temperature to 400 and 500 °C results in the generation of additional, weaker acid sites, as evidenced by the emergence of a peak at 175 °C and 145 °C in 10Ni/Ti-M_400 and 10Ni/Ti-M_500, respectively. In contrast, the 10Ni/Ti-A catalyst exhibited analogous peak profiles (Fig. 5b). However, a distinction emerged in the peak areas among the three calcined catalysts. The 10Ni/Ti-A_300 catalyst was found to possess the highest acid sites, with a value of 253 μmol g^{-1}. It was observed that the total number of acid sites decreased with an increase in the calcination temperature, which is attributed to the decrease in surface area. Specifically, the contribution of weak acid sites exhibited a decline from 55% to 42%, while the contribution of medium acid sites exhibited an increase from 45% to 54% with an increase in the calcination temperature.

The rutile-based catalysts exhibited distinct peak profiles in comparison with anatase and mixed-phase titania (Fig. 5c). The total acidity exhibited a decrease from 144 to 117 μmol g^{-1} with increasing calcination temperature from 300 to 400 °C and further increased to 201 μmol g^{-1} for the 500 °C calcined catalyst. It is noteworthy that medium acid sites contribute approximately to 60% of the total acidity. The observed discrepancy in total acidity can be attributed to the elevated surface area of the three titania at varying calcination temperatures, which exhibits a considerably higher concentration of accessible acidic sites, even following the nickel dispersion.

The loading of nickel exerts an influence on the acidic sites, particularly those of a relatively weaker nature. A decrease in nickel loading from 10 wt% to 5 wt% results in an increase in weak acidic sites, with an associated decrease in medium acidic sites (Fig. S7 and Table 2, entries 4, 8 and 12).

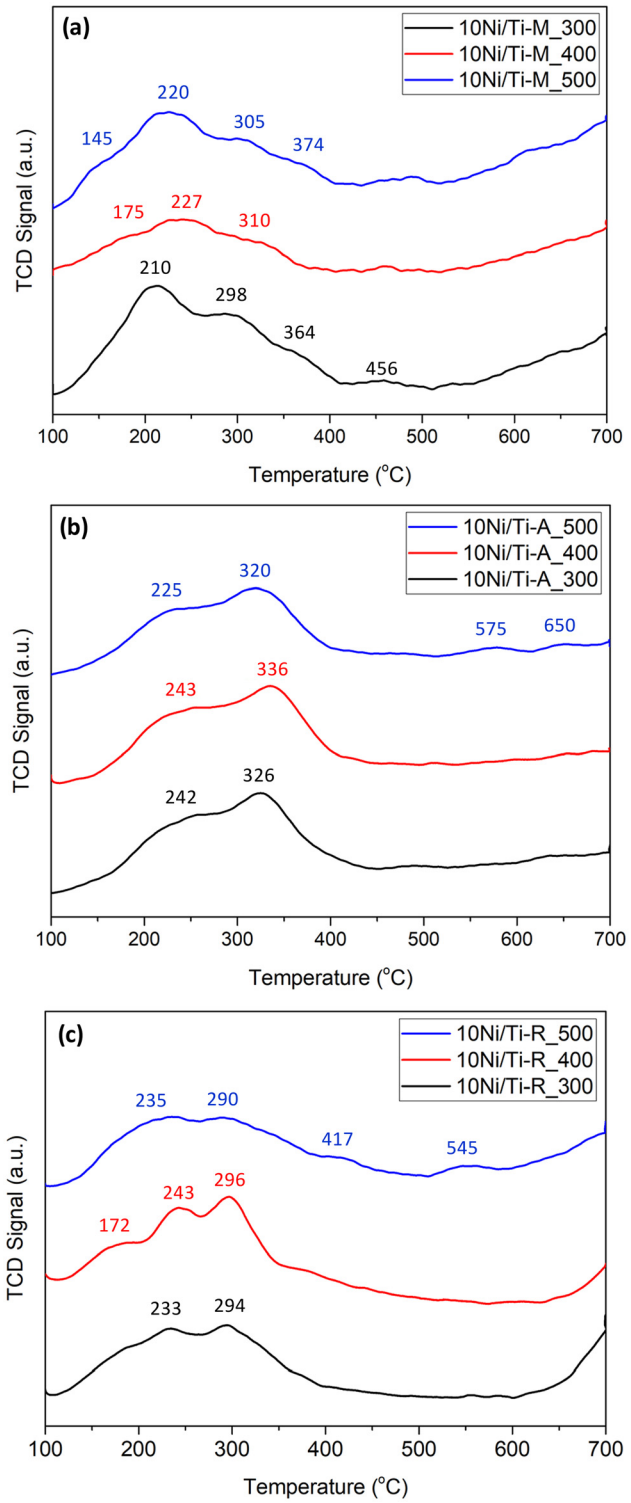

Fig. 5 NH_3-TPD profiles of (a) 10Ni/Ti-M, (b) 10Ni/Ti-A, and (c) 10Ni/Ti-R calcined at different temperatures.

Nevertheless, the total acidity was observed to decrease with increasing nickel loading and this reduction can be attributed to an increased coverage of the titania surface by nickel species.

TEM imaging

Fig. 6 shows transmission-electron microscopy (TEM) images of nickel-supported catalysts. The titania Ti-M sample exhibited an irregularly shaped morphology with a relatively dense nickel distribution. The histogram revealed that the nickel distribution ranged from 10 to 30 nm, with an average particle size of 18.5 nm. The Ti-A titania exhibited a regular tablet-shaped morphology with nickel particle distribution between 4 and 10 nm. It is challenging to discern the individual nickel particles from the Ti-M and Ti-A titania supports due to the contrast differences between the particles and the supports. However, the presence of Ni nanoparticles was notably discernible on rutile titania (Ti-R). The rutile-based catalyst (10Ni/Ti-R_500) exhibited rod-shaped titania of 80–200 nm length and 20–30 nm width, with a Ni particle size distribution between 5 and 13 nm.

The difference in particle sizes can be attributed to variations in surface area. Indeed, the particle sizes decrease as the surface area increases, following the order: 10Ni/Ti-A_500 (S_{BET} = 78 m^2 g^{-1}, d_{TEM} = 7 nm), 10Ni/Ti-R_500 (S_{BET} = 51 m^2 g^{-1}, d_{TEM} = 8 nm) and 10Ni/Ti-M_500 (S_{BET} = 40 m^2 g^{-1}, d_{TEM} = 19 nm). As observed, Ti-A and Ti-R titania generated small Ni particle sizes, which are generally considered to be active sites for catalytic hydrogenation. Furthermore, it can be inferred that the properties of the titania surface govern the growth of the Ni particles.

X-ray photoelectron spectroscopy (XPS)

XPS was performed to study the electronic state of Ni in the reduced catalysts calcined at different temperatures. The resulting spectra (Ni 2p and O 1s) are shown in Fig. 7, while the quantitative analysis of Ni, Ti, and O species in various chemical states, along with their binding energies and percent area, is outlined in Table S3. For the sake of clarity, only the Ni $2p_{3/2}$ domain corresponding to binding energies in the range of 850 to 869 eV is shown. All the spectra exhibited characteristic peaks for nickel and its oxides, accompanied by satellite peaks. It is noteworthy that although the reduced catalysts were submitted for analysis, the nickel might have undergone partial oxidation during the transfer of the samples. Consequently, a mixture of Ni^0 and Ni^{2+} peaks at ~852 and ~854 eV, respectively, is observed. The peak at ~856 eV corresponds to a broad peak comprising a mixture of Ni_2O_3, $Ni(OH)_2$ and Satellite 1 of NiO.[53,54] Among the three titania catalysts calcined at 500 °C, the highest surface nickel was observed in the 10Ni/Ti-R_500 catalyst, followed by 10Ni/Ti-M_500 and 10Ni/Ti-A_500 catalysts (see Table S3, entries 3, 6, and 7). However, it is crucial to note that the calcination temperature exerts a substantial influence on the Ni/Ti ratio. For instance, the 10Ni/Ti-M_300 catalyst exhibited a Ni/Ti ratio of 0.21, which decreased with an increase in calcination temperature (Fig. S8). A considerable corpus of research has demonstrated that the behaviour of nickel particle size reduction, the characteristics of nickel oxide, and the surface of the support are factors that have proven to influence the surface Ni/Ti

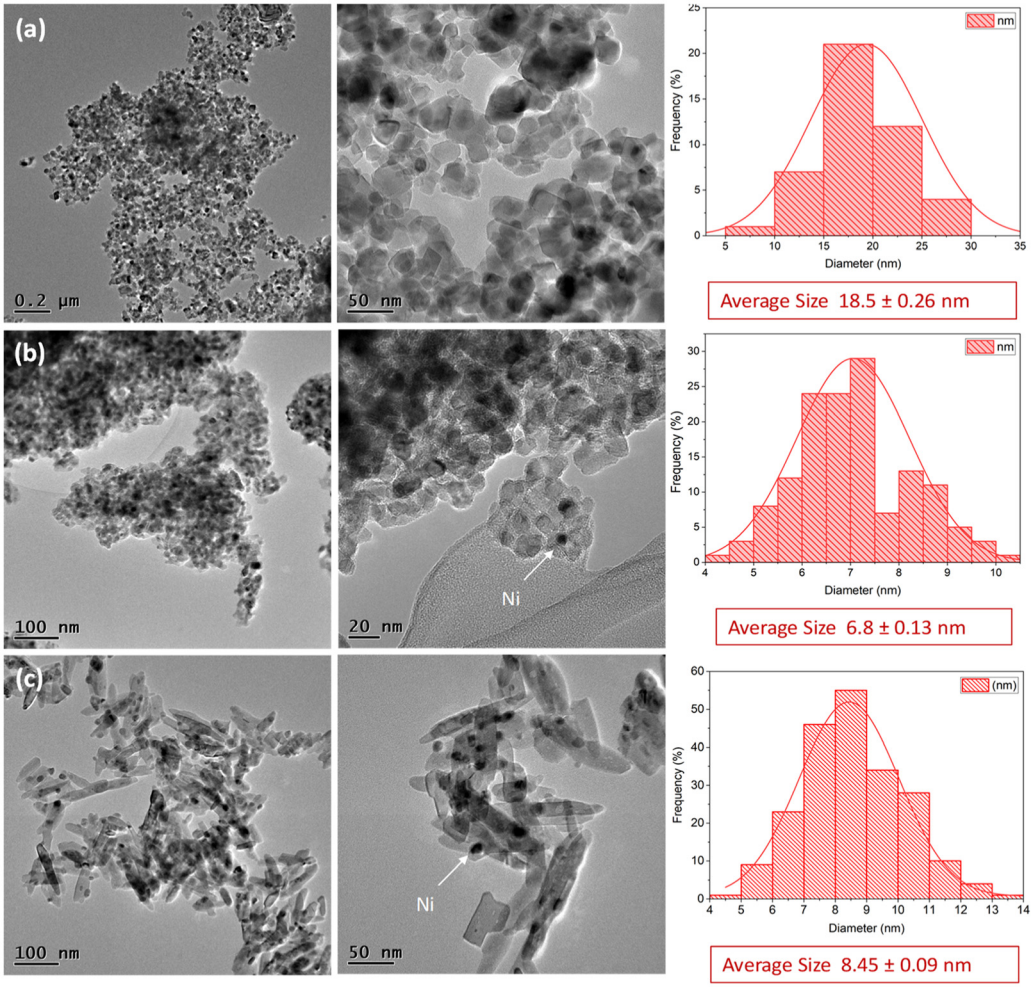

Fig. 6 TEM images and histograms of Ni nanoparticles in (a) 10Ni/Ti-M_500, (b) 10Ni/Ti-A_500, and (c) 10Ni/Ti-R_500 catalysts.

ratios.[34,55] In addition, the broadening of peaks of Ni $2p_{3/2}$ is dependent on the presence of oxygen deficiency and/or interaction of nickel atoms with their neighbouring atoms.[53] Notably, the Ni^0 peak is slightly shifted to a lower binding energy for the rutile phase catalyst (851.8 eV) compared to mixed and anatase phase-based catalysts (852.0 and 851.9 eV). This value is lower than the binding energy of standard Ni metal (852.6 eV). The shift to a lower binding energy indicates the presence of electron-rich Ni species ($Ni^{\delta-}$) and possibly a charge transfer between the metal and the support. The amount of Ni^0 follows the order 10Ni/Ti-M_500 > 10Ni/Ti-A_500 > 10Ni/Ti-R_500. These results follow the same trend as the degree of reduction (%Red.) obtained by TPR (Table 2) where the Ni phase was less reduced when supported on the rutile support (Ti-R).

As per the standard values, the binding energies of lattice oxygen in hydroxide, Ni_2O_3, NiO and TiO_2 are observed at 531.2, 531.8, 529.6 and 529.9 eV, respectively.[56] The deconvoluted O 1s core level spectra of the three titania catalysts, as depicted in Fig. 7 (right), showed a big peak at ~529 eV, which is associated with oxygen bonded to the metal lattice site (TiO_2/NiO), and a short broad peak at approximately 531 eV, which is indicative of amalgamation of surface hydroxyl and Ni_2O_3. From Table S3 and Fig. S8, it can be deduced that the calcination temperature appears to exert minimal influence on the binding energies of oxygen in NiO/TiO_2 and $Ni(OH)_2$/Ni_2O_3, with values of approximately 529.7 and 531.1 eV observed for the majority of the samples. However, a deviation from this trend is noted for the 10Ni/Ti-A_300 catalyst, where the binding energies are observed at 530.5 and 531.9 eV. This shift to a higher binding energy is attributed to electron transfer to atoms neighbouring the oxygen vacancies.[57] The results also suggest a slightly higher amount of $Ni(OH)_2$ in the anatase catalysts.

In summary, the characterization results demonstrated that thermal treatment exerts a significant impact on the surface properties of titania. Anatase-based catalysts exhibited the greatest surface area and higher charge transfer. Furthermore, XRD analysis revealed the formation of larger nickel oxide and nickel particles in the mixed Ni/Ti-M catalysts in contrast to anatase (Ni/Ti-A) and rutile (Ni/Ti-R)-based catalysts. The impact of calcination temperature on crystallite size was not significant in the case of Ni/Ti-A and Ni/Ti-R catalysts.

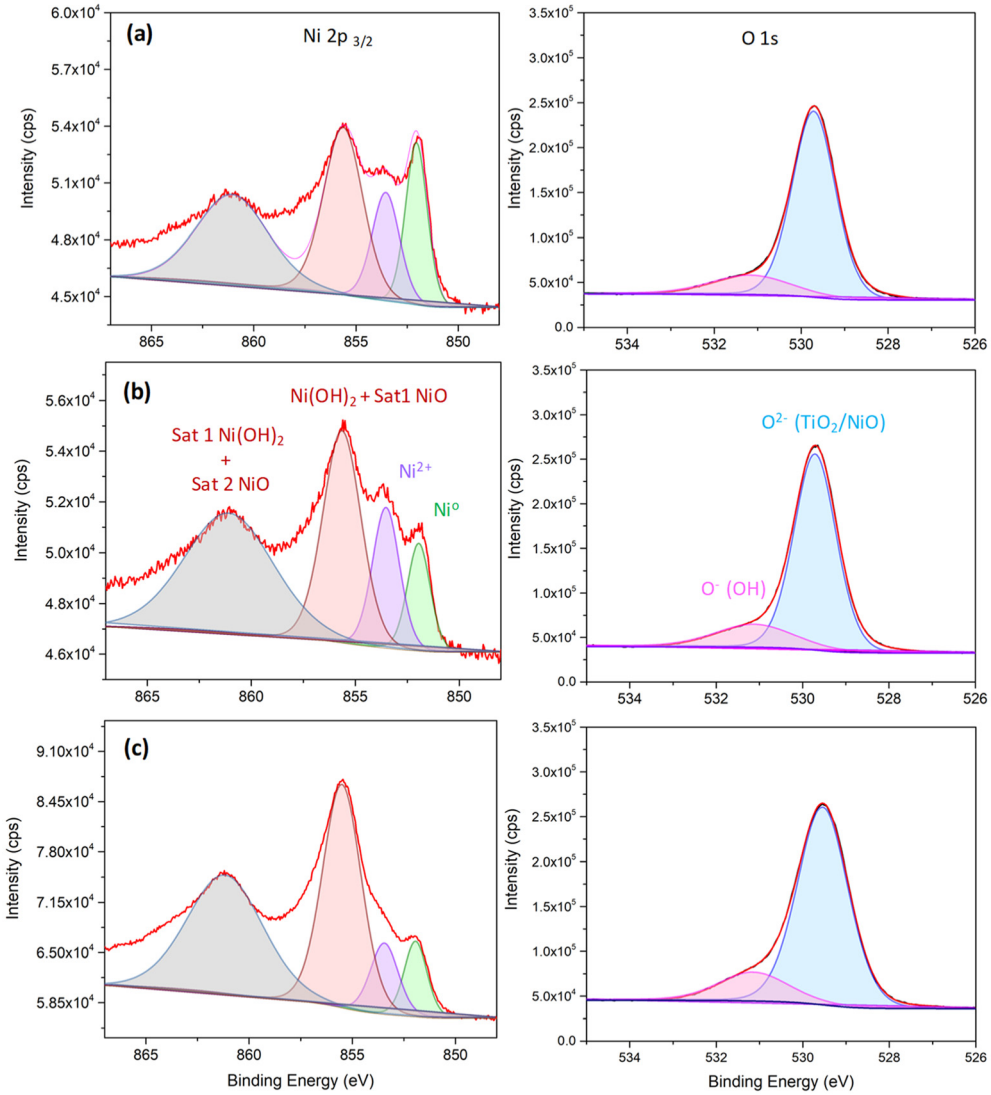

Fig. 7 XPS spectra of the Ni catalysts. Ni 2p (left) and O 1s core level spectra (right) of (a) 10Ni/Ti-M_500, (b) 10Ni/Ti-A_500 and (c) 10Ni/Ti-R_500 catalysts.

Similarly, the TEM results indicated that the presence of a mixed phase of titania resulted in the formation of larger nickel particles compared to those formed with Ti-R rutile and Ti-A anatase supports. Additionally, the reduction profiles indicated that the anatase phase facilitated a homogeneous reduction of nickel oxide at lower temperatures. Both mixed and anatase phase catalysts demonstrated full reduction of the nickel oxide. In contrast, rutile phase-based catalysts exhibited a lower degree of reduction (80%) due to higher metal–support interactions. Among the three titania catalysts, the anatase catalyst exhibited the highest number of acidic sites, and these sites exhibited a decrease in strength with increasing calcination temperature. The 10Ni/Ti-R_500 catalyst demonstrated a substantial surface nickel content, and the calcination effect exerted a moderate influence on the surface nickel-to-titania ratio, as evidenced by XPS experiments.

Catalytic performance

As discussed in the characterization section, the calcination temperature and nature of the support have a great impact on the surface acidity and the structural (particle size and porosity) and chemical (metal–support interaction) properties of the catalyst. To gain insight into the catalytic performances of the catalysts, the effect of reaction time and temperature on the three titania-supported catalysts (10Ni/Ti-M, 10Ni/Ti-A, and 10Ni/Ti-R) was studied. The hydrogenation reactions were performed at 30 °C for 2, 4, and 6 hours (Table S4) and at 50 °C for 2 and 4 hours (Table S5). Fig. 8 presents the time dependent conversion of MBY and the product yield. A control experiment was performed with the supports alone to determine the role of nickel species in the hydrogenation of alkynols. The absence of conversion demonstrates that the nickel species were the active component in this process (Table S4,

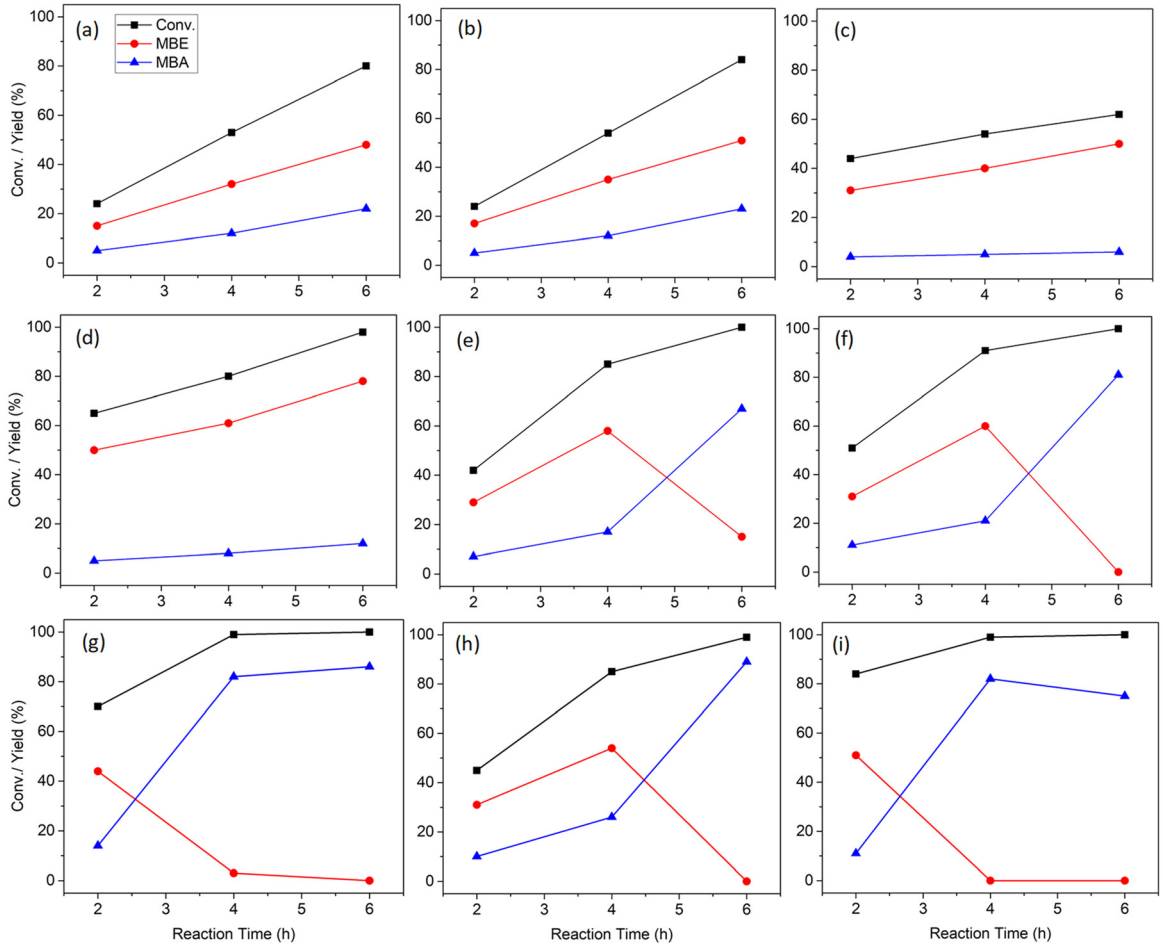

Fig. 8 Catalytic conversion with product distribution for different reaction times at 30 °C for (a) 10Ni/Ti-M_300, (b) 10Ni/Ti-M_400, (c) 10Ni/Ti-M_500, (d) 10Ni/Ti-A_300, (e) 10Ni/Ti-A_400, (f) 10Ni/Ti-A_500, (g) 10Ni/Ti-R_300, (h) 10Ni/Ti-R_400, and (i) 10Ni/Ti-R_500 catalysts. Reaction conditions: MBY – 1 g, H_2O – 40 g, catalyst – 100 mg, temp. – 30 °C, time – 6 h, H_2 – 10 bar (at 30 °C), and RPM – 900.

lines 1–9). Fig. S9 shows the reaction pathway of the hydrogenation of MBY and the possible products.

The nature of the support and the calcination temperature have a strong impact on the catalytic results. As expected, an increase in the MBY conversion between 2 h and 6 h of reaction was observed for all the catalysts. At 30 °C and 6 h, the conversions are nearly complete for 10Ni/Ti-A and 10Ni/Ti-R, while they remain below 84% for 10Ni/Ti-M. The calcination temperature of the catalysts affects the conversion. Notably, the catalysts calcined at lower temperatures (300 °C and 400 °C) for Ti-M and Ti-A exhibited higher conversions than those calcined at 500 °C. For each calcination temperature, the TON at 2 h (Table S4) follows the order 10Ni/Ti-M < 10Ni/Ti-A < 10Ni/Ti-R. When plotting TON as a function of crystallite size (Fig. S10), it appears that the activity increases with decreasing Ni crystallite size for a specific calcination temperature.

For all the catalysts, MBE is formed as the predominant product with MBA as the by-product for conversion up to 95%. For 10Ni/Ti-M, MBE is always the primary product, with selectivity in the range of 60–81%. The MBY conversion goes up to 84%, associated with an MBE yield of 51%. Regarding 10Ni/Ti-A and 10Ni/Ti-R, the yield of MBE also increases with conversion. It is worth noting that the selectivity to MBE at *ca.* 80% conversion for titania (Ti-M, Ti-A, Ti-R) supported Ni catalysts calcined at 400 °C is in the same range (61–68%). However, for the catalysts calcined at 500 °C, the selectivity to MBE is higher for 10Ni/Ti-A-500, which generates the highest yield of MBE (78%) at 6 h. Once full conversion is achieved, a switch of selectivity towards MBA is observed. This suggests competitive adsorption of MBY and MBE and the successive reaction is promoted once MBY has completely disappeared. This is attributed to the excessive adsorption of the reactant MBY, as evidenced by complementary experiments and analyses in section 3.2.1. The highest yields of MBA on the different supports are obtained with 10Ni/Ti-A_300 (81%) and 10Ni/Ti-R_400 (89%), at 6 h. Furthermore, a prolonged reaction time appears to generate the other by-products (not detected in GC), thereby compromising the mass balance (Table S4). The formation of other by-products such as acetone and methyl butene can be ruled out because they are usually formed at

Table 3 Key structural properties and catalytic performance of three titania catalysts

S. no.	Catalyst	Ni[a] (wt%)	S_{BET}[b] ($m^2\ g^{-1}$)	d_{Ni}[c] (nm)	Acid sites[d] ($\mu mol\ g^{-1}$)	MBY conv. %	Yield (%) MBE	MBA	TON
1	10Ni/Ti-M_500	9.5	40	24	145	62	50	6	46
2	10Ni/Ti-A_500	9.3	78	11	211	98	78	12	74
3	10Ni/Ti-R _500	11.1	51	12	201	100	0	75	63

[a] Measured by ICP-OES. [b] BET surface area. [c] Average crystallite size of Ni calculated using the Scherrer equation. [d] Obtained from NH_3-TPD analysis. Reaction conditions: MBY – 1 g, H_2O – 40 g, catalyst – 0.1 g, temp. – 30 °C, time – 6 h, H_2 – 10 bar (at 30 °C), and RPM – 900.

higher temperatures.[32] Table 3 summarizes the key structural properties and catalytic performances of the three titania catalysts.

The reactions were also conducted at 50 °C where all catalysts exhibited near-complete MBY conversion within four hours (Table S5). The yields of MBE are lower in comparison with the reactions at 30 °C. For example, the highest yields of MBE reached 38% (*vs.* 51% at 30 °C) for 10Ni/Ti-M and 68% (*vs.* 78% at 30 °C) for 10Ni/Ti-A. These may be attributed to a higher activation energy for the hydrogenation of MBE to MBA than that for MBY to MBE, as previously reported in the literature.[58] The highest yields of MBA (83–86%) are similar to those obtained at 30 °C. A reaction was also conducted at atmospheric pressure with 10Ni/Ti-M but this resulted in low conversion (13%, Table S4).

Additionally, low nickel loading catalysts (5 wt%) were examined for Ti-M, Ti-A and Ti-R at 30 and 50 °C temperatures; the results are presented in Fig. S11 and the data are compiled in Tables S4 and S5. As expected, the conversion at 30 °C is lower with 5Ni/Ti than with 10Ni/Ti catalysts, but the TON is higher. It is worth noting that the TON follows the same order as observed previously: 10Ni/Ti-M < 10Ni/Ti-A < 10Ni/Ti-R. The MBY conversion increased gradually from 24% to 66% with the 5Ni/Ti-M_500 catalyst and the yields to MBE were relatively moderate (42% at 6 h). In comparison, 5Ni/Ti-A_500 exhibited superior activity and elevated MBE yields (71% at 6 h). 5Ni/Ti-R_500 showed MBA as a dominant product in 46% yield at 90% conversion. As illustrated in Fig. S11b, when the reaction temperature was raised to 50 °C, the activity of the nickel catalysts increased and full conversion was obtained with the three supports after 4 h, which resulted in the formation of MBA as a major product in yields ranging from 68 to 75%.

In order to illustrate the surface sensitivity of the titania-based catalysts, catalytic reactions were conducted in the presence of a quinoline additive. Quinoline is typically employed in conjunction with Pd–Pb/$CaCO_3$ in the selective hydrogenation of alkynes at an industrial scale. The primary function of quinoline is to polarize the Pd–H bond in the vicinity of the catalyst surface by donating electrons. However, in this study, when 10% quinoline with respect to MBY was employed, the results differed markedly for all three catalysts. The results demonstrate a significant improvement in conversion for Ti-M-based catalysts, whereas a decline was observed for Ti-A and Ti-R based catalysts (Fig. S12). Moreover, at a similar conversion (82–84%), the selectivity to MBE is much higher for 10Ni/Ti-R-500 in the presence of quinoline (*ca.* 82% *vs.* 61%) and 67% yield of MBE was obtained. One potential explanation for these differences is the varying degrees of interaction between quinoline and the supports, which is not the focus of this study. Finally, a Lindlar catalyst was subjected to analogous reaction conditions (30 °C) and exhibited nearly 100% conversion, with the formation of MBA as the predominant product (86% at 6 h) (Table S4, entries 52–54). A comparative analysis of the extant literature yielded results indicating a superior yield in MBE in our case (Table 1).

Understanding the role of titania phases and the mechanistic pathway

It is widely acknowledged that the hydrogenation of alkynes or alkynols is a structure-sensitive reaction,[59,60] whereby the distribution of products is contingent upon the inherent characteristics of the titania surface and the nature of the species present. Furthermore, the surface properties of the support, including acidic/basic site densities, surface area, vacancies, and defects, can exert a significant influence on the overall activity and product distribution.

As evidenced in the literature,[3] the selective semi-hydrogenation of alkyne/alkynol to alkene/alkenol over heterogeneous catalysts can be governed by two factors: thermodynamic and mechanistic.[61] When the hydrogenation of alkyne/alkynol is favoured over that of alkene/alkenol, the mechanistic pathway exerts a dominant influence. In contrast, if the rates of hydrogenation of alkene are higher than those for the hydrogenation of alkyne, a high selectivity to alkene is then attributed to thermodynamic factors. In this case, the selective adsorption of alkyne/alkynol in the presence of alkene will inhibit the over-hydrogenation step to the alkane. This preferential interaction of MBY with the surface, to the detriment of MBE, has previously been reported for Pd and Cu catalysts.[32,58] Therefore, the employment of a catalyst with a higher affinity for the adsorption of alkynes or alkynols relative to alkenes will result in a higher level of alkene/alkenol selectivity.

In order to illuminate the pathway, hydrogenation of MBE to MBA was performed separately under analogous reaction conditions with 10Ni/Ti-M_500, 10Ni/Ti-A_500, and 10Ni/Ti-R_500 catalysts. Fig. 9 compares the conversion of MBY and the conversion of MBE as a function of reaction time at 30 °C.

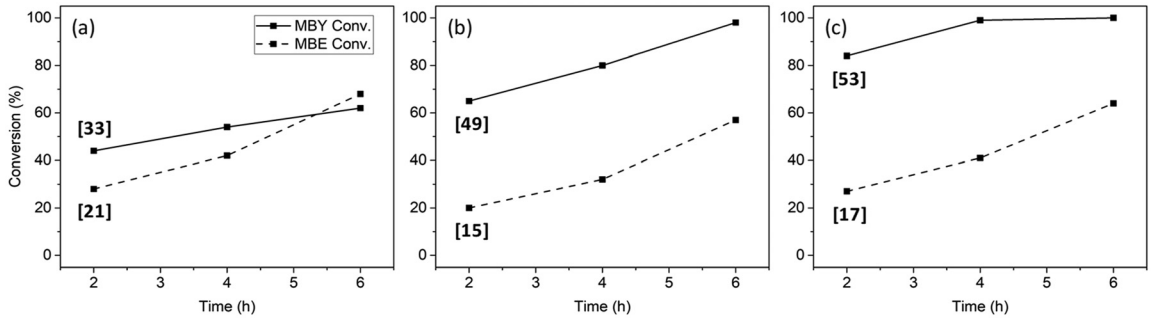

Fig. 9 Conversion of MBY and MBE for (a) 10Ni/Ti-M_500, (b) 10Ni/Ti-A_500, and (c) 10Ni/Ti-R_500 catalysts. The numbers in square brackets represent TON at 2 h. Reaction conditions: reactant – 1 g, H_2O – 40 g, catalyst – 100 mg, temp. – 30 °C, time – 2–6 h, H_2 – 10 bar (at 30 °C), and RPM – 900.

For the 10Ni/Ti-M_500 catalyst, the hydrogenation of MBE was comparable to that of MBY (Fig. 9a). Conversely, in the case of 10Ni/Ti-A_500 and 10Ni/Ti-R_500 catalysts, hydrogenation of MBY was much faster (by a factor of 2 and 3) than that of MBE. This observation indicates that anatase and rutile catalysts exhibit a greater propensity for hydrogenating MBY to MBE than MBE to MBA; therefore, the mechanistic pathway is the dominant pathway. These might be linked to the lower Ni crystallite sizes for 10Ni/Ti-A and 10Ni/Ti-R.

To elucidate further the pathway and the parameters controlling the selectivity in anatase (Ti-A), mixed (Ti-M) and rutile titania (Ti-R) catalysts, the desorption of MBY was investigated on the reduced catalysts by vapor-flow-TPD experiments. To achieve this, a known quantity of catalyst is reduced under hydrogen at 500 °C. Once the temperature reaches 40 °C (near the reaction temperature of 30 °C), the reactant MBY is allowed to adsorb on the reduced catalyst through a flow of He saturated with MBY. Finally, once the physisorbed MBY has been removed, its desorption is recorded as a function of temperature and quantified using TPD experiments. Fig. 10 presents the desorption profiles of MBY on different titania catalysts, while Table S6 lists the quantity of MBY desorbed from the catalysts. The results demonstrate that the anatase-based catalysts showed the highest desorption (90–158 μmol g^{-1}), followed by 10Ni/Ti-R (64–70 μmol g^{-1}) and then 10Ni/Ti-M (54–62 μmol g^{-1}). The overall affinity for MBY adsorption among the Ni/Ti-M and Ni/Ti-R-based catalysts was found to be relatively similar for different calcination temperatures. Consequently, the product distribution remained comparable for the three calcination temperatures. However, the calcination temperature had an impact on the adsorption of MBY on the Ni/Ti-A surface. An increase in the calcination temperature from 300 °C to 500 °C was found to result in a decrease in the adsorption of MBY, from 158 μmol g^{-1} to 90 μmol g^{-1}. These were associated with an increase in selectivity to MBE (from 60% to 80%), to the detriment of MBA. The variation of the affinity for MBY depending on the catalyst follows the same trends as for the acidity, which suggests a direct correlation. The existence of coordinately unsaturated surface Ti ions, which are responsible for the acidic sites, has been observed to be higher in anatase-based catalysts. These sites have the potential to enhance the adsorption of alkynols, thereby contributing to the capture and strengthening of the adsorption process. In agreement with the literature, the excessive adsorption of MBY results in the coverage of active sites on the catalyst surface, which prevents the hydrogenation of MBE to MBA. This is why near full conversion of MBY has to be achieved before the successive reaction to MBA can occur, notably on 10Ni/Ti-A. Totarella *et al*. also reported in their work that 100% MBE selectivity at 50% MBY conversion was due to preferential interaction of MBY with the surface of Cu rather than MBE.[32]

The highest yield of MBE was obtained with 10Ni/Ti-A_500. Based on the characterization, different properties must have played a role. There is an enhanced adsorptive capacity in anatase-based catalysts, as evidenced by MBY-TPD experiments, which demonstrate higher adsorption capability compared to mixed-phase titania catalysts. Furthermore, the enhanced charge transfer from titania to nickel in Ti-A catalysts, as determined by UV-Vis analysis, renders metal species more nucleophilic, thereby enhancing the greater affinity towards the reactant (alkynes) and hydrogen compared to Ti-M-based and Ti-R catalysts. Furthermore, the TPR results indicated that nickel oxide species in anatase-based titania are more susceptible to reduction compared to other catalysts. Finally, XPS results also confirmed the presence of electron-rich Ni species ($Ni^{\delta-}$) in anatase-based catalysts. In light of the aforementioned observations and facts, a straightforward mechanistic pathway is presented in Fig. 11, which illustrates the formation of different products. The reaction mechanism is similar to that reported for semi-hydrogenation of alkynes and follows the Langmuir–Hinshelwood mechanism.[4,62] In brief, the sequence of events that occur in the context of the reaction mechanism is as follows: the initial step involves the co-adsorption of reactants on the surface, which is followed by the dissociative adsorption of dihydrogen species on nickel species. Concurrently, the reactant undergoes adsorption on a surface that is coordinately unsaturated with titanium ions. In the course of the reaction, the subsequent addition of H atoms to the adsorbed alkynol results in the formation of alkenol. Subsequently, the formed alkenol is desorbed from the

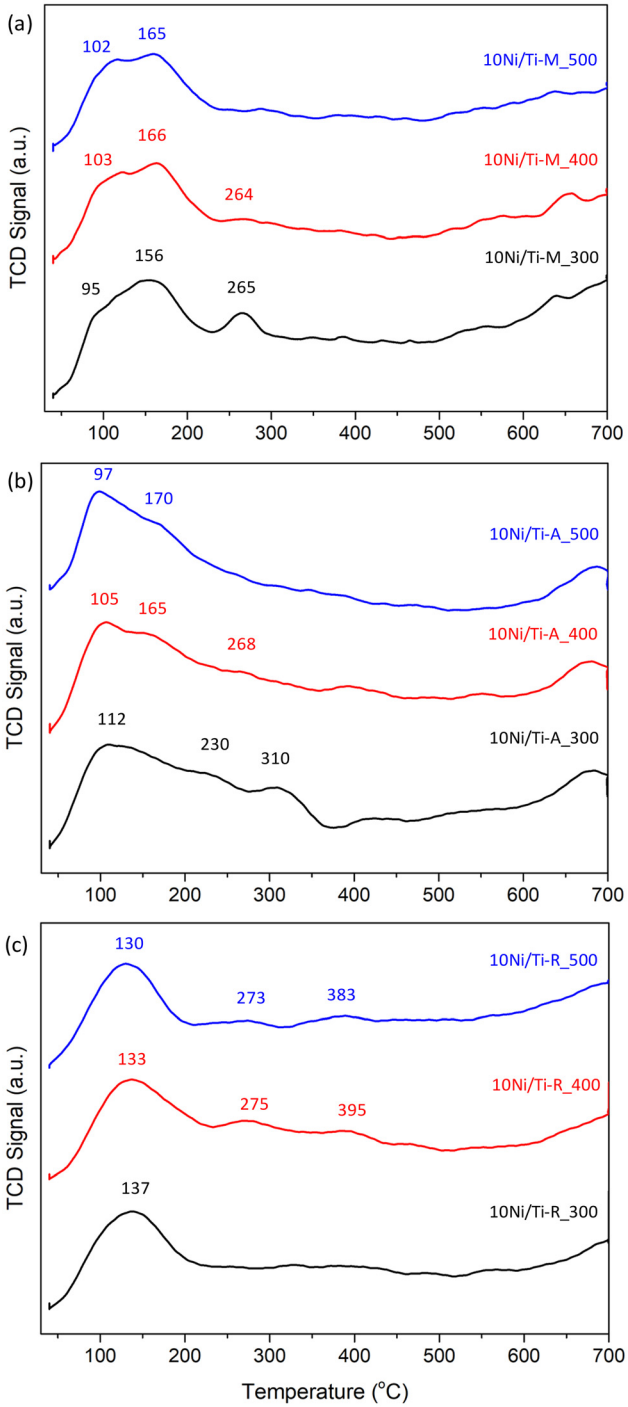

Fig. 10 MBY desorption profiles of (a) 10Ni/Ti-M, (b) 10Ni/Ti-A, and (c) 10Ni/Ti-R-based catalysts calcined at different temperatures.

surface. The propensity of anatase-based catalysts to adsorb MBY hinders the overhydrogenation of MBE to MBA, thereby ensuring high MBE selectivity. The phenomenon is governed by metal–support interactions, nickel oxide reduction behavior, and the presence of electron-rich Ni species on the titania support. In essence, the product distribution during nickel-catalyzed hydrogenation of alkynols is found to be predominantly contingent upon the adsorption characteristics of the alkynol on the catalyst surface, the nickel species present, and the acidity of the support.[3]

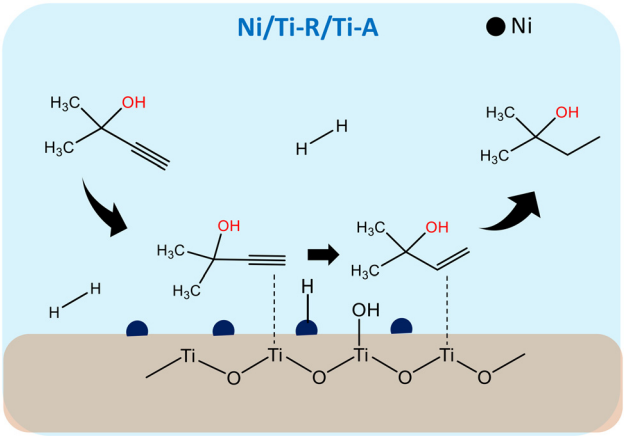

Fig. 11 Reaction pathways in MBY semi-hydrogenation over the supported Ni catalyst.

Recycling study

To further assess the stability of the catalyst, recycling tests were performed with 10Ni/Ti-M_500 and 10Ni/Ti-A_500 at 30 °C and 10 bar H_2 for 6 h. Subsequent to the initial run, the catalyst was retrieved by centrifugation and subjected to overnight drying at 80 °C. For the second run, the catalyst was either used directly after drying (Reused_dried) or after calcination and reduction at 500 °C for 2 h (Reused_red). Fig. 12 and Table S4 present the comparative analysis of the fresh and reused (dried and reduced) catalysts. In the case of the 10Ni/Ti-M catalyst, after 6 h, the MBY conversion increased from 62% to 72–74% with both dried and reduced catalysts. It is worth noting that 10Ni/Ti-M_500 exhibits the same results after drying as it does after the supplementary heat treatment (reduction). In contrast, a 10–12% drop in the MBY conversion was observed for 10Ni/Ti-A (from 98% to 86–88%). However, for both catalysts, the selectivity to MBE decreased slightly from *ca.* 80% to 50–60%.

Chemical analysis of the reused catalyst revealed no significant nickel loss after the two runs. To ascertain whether coke formation occurs during the semi-hydrogenation reaction, TGA profiles of dried reused catalysts were obtained. The thermal profiles of the dried catalysts (Fig. 12b) show two weight losses in the low and high temperature regions. In the temperature range of 100 to 150 °C, both the catalysts exhibited a weight loss of approximately 3%, which can be attributed to the presence of physically adsorbed water. A weight loss of ~2% in the temperature range of 250–450 °C in Ni/Ti-A can be attributed to the combustion of organic carbon. However, the Ni/Ti-M reused catalyst exhibited a gain in mass of 0.3%, which may be attributed to the reoxidation of pre-existing reduced Ni species in the catalyst, followed by a subsequent

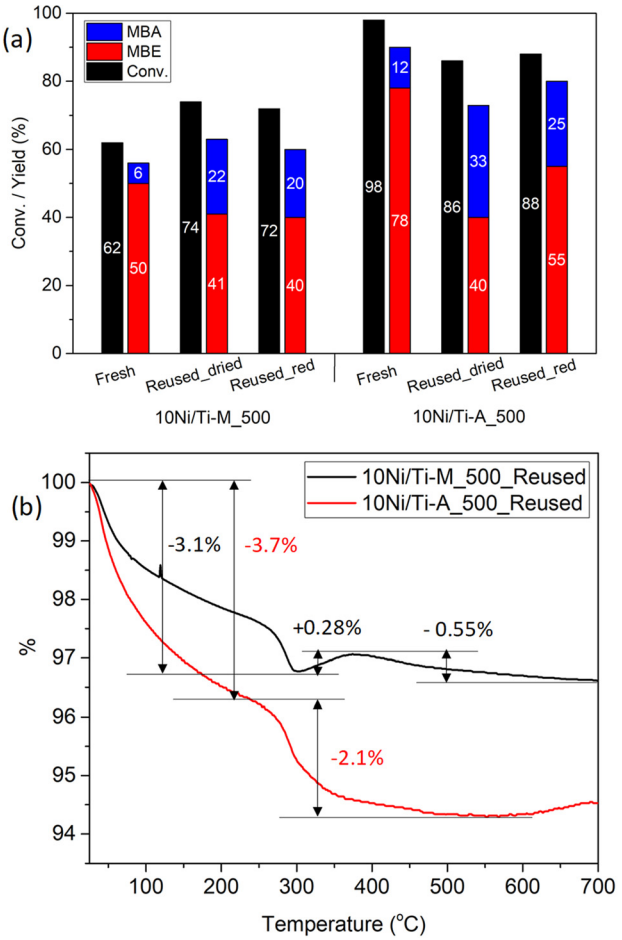

Fig. 12 Ni-titania catalysts: (a) recycle tests at 30 °C for 6 h and (b) TGA.

weight loss of 0.5%. This suggests the presence of deposited carbon in the reused catalyst, especially for Ni/Ti-A.

XRD patterns of the calcined reused catalyst are shown in Fig. S13. The crystallite size of nickel in the Ni/Ti-M catalyst decreased from 24 nm to 19 nm with minimal variation in the anatase and rutile phase composition. A decrease in nickel crystallite size may be attributed to the formation of a solid solution of nickel oxide with the support and anchoring effect, which has been previously reported in the literature to prevent the sintering of nickel particles during the second calcination and the reduction step.[63] We previously showed that the activity increases with decreasing Ni crystallite size, which explains the increase in conversion after recycling. In contrast, the crystallite size of nickel remains unaltered (11 nm for fresh *vs.* 11 nm for reused) for the Ni/Ti-A catalyst. Furthermore, the anatase titania exhibited no change in the lattice parameters, thereby confirming the robustness of the Ni/Ti-A catalyst after the reaction.

The reduction profiles of both reused catalysts are shown in Fig. S14. Notably, the reused Ni/Ti-M catalyst exhibits lower reduction behavior than the fresh catalyst with a reduction temperature of 352 °C compared to 412 °C, and a reduction of NiO to approximately 100%. The shift of the reduction peak to a lower temperature indicates a change in the metal–support interaction following the reaction. In contrast, the reused Ni/Ti-A catalyst exhibited a similar reduction peak compared to the fresh catalyst (350 *vs.* 367 °C), indicating enhanced stability of the Ni particles. However, the reduction peak of NiO was broader and accompanied by elevated hydrogen consumption levels (1724 μmol g^{-1}) in comparison with the theoretical value of 1686 μmol g^{-1}. Therefore, some coke remaining on the surface must be hydrogenated. Some active sites must be blocked, even after thermal treatment, which would explain the lower conversion for the reused Ni/Ti-A catalyst.

Conclusions

In summary, the present study examined the effects of varying anatase and rutile compositions, calcination temperatures, and metal loadings on the performance of heterogeneous Ni/TiO_2 catalysts in the selective hydrogenation of MBY to MBE. The findings of this study suggest that the calcination temperature and the anatase/rutile phases of the catalyst appear to influence the metal–support interaction, reducibility, surface nickel species, and the adsorption of MBY. Ni/TiO_2 catalysts were active for the semi-hydrogenation of MBY to MBE under mild conditions (30 °C, 10 bar H_2). The Ni size was shown to have a strong effect on the activity. Based on the results, we demonstrated that the reaction follows primarily a mechanistic pathway for the anatase Ni/Ti-A and rutile Ni/Ti_R catalysts. However, the selectivity to the alkenol depends also on the acidity and MBY adsorption capabilities, which are higher for the anatase supported Ni catalysts. Finally, the highest yield of MBE (78%) was obtained with 10Ni/Ti-A_500.

Author contributions

Ajay Tomer: conceptualization, methodology, investigation, and writing – original draft, review & editing. Laurent Djakovitch: funding acquisition, conceptualization, supervision, investigation, and writing – review & editing. Noémie Perret: funding acquisition, project administration, conceptualization, supervision, investigation, and writing – review & editing.

Conflicts of interest

There are no conflicts to declare.

Data availability

All the data supporting this article have been included as part of the SI. Supplementary information is available. See DOI: https://doi.org/10.1039/d5gc03626g.

Acknowledgements

The authors would like to acknowledge the scientific platform IRCATECH of IRCELYON for their assistance in the characterization of the catalyst. Anne Bonhomme of IRCELYON is thanked for conducting the UV-Vis analysis. Pascale Mascunan and Nicolas Bonnet of IRCELYON are acknowledged for performing the ICP-OES measurements. This work was supported by a government grant managed by the Agence Nationale de la Recherche under the France 2030 program, with reference ANR-22-PESP-0006.

References

1 W. Bonrath, J. Medlock, J. Schutz, B. Wustenberg and T. Netscher, in *Hydrogenation*, ed. I. Karam, InTech, 2012.
2 W. Bonrath, M. Eggersdorfer and T. Netscher, *Catal. Today*, 2007, **121**, 45–57.
3 X. Chen, C. Shi and C. Liang, *Chin. J. Catal.*, 2021, **42**, 2105–2121.
4 X. Deng, J. Wang, N. Guan and L. Li, *Cell Rep. Phys. Sci.*, 2022, **3**, 101017.
5 M. Sk, S. Haldar, S. Bera and D. Banerjee, *Chem. Commun.*, 2024, **60**, 1517–1533.
6 P. Wang, Y. Ma, Y. Shi, F. Duan and M. Wang, *Materials*, 2023, **16**, 7409.
7 Y. Yang, X. Zhu, L. Wang, J. Lang, G. Yao, T. Qin, Z. Ren, L. Chen, X. Liu, W. Li and Y. Wan, *Nat. Commun.*, 2022, **13**, 2754.
8 G. Vilé, N. Almora-Barrios, S. Mitchell, N. López and J. Pérez-Ramírez, *Chem. – Eur. J.*, 2014, **20**, 5926–5937.
9 H. Lindlar, *Helv. Chim. Acta*, 1952, **35**, 446–450.
10 A. Yarulin, I. Yuranov, F. Cárdenas-Lizana, D. T. L. Alexander and L. Kiwi-Minsker, *Appl. Catal., A*, 2014, **478**, 186–193.
11 N. Cherkasov, A. O. Ibhadon, A. J. McCue, J. A. Anderson and S. K. Johnston, *Appl. Catal., A*, 2015, **497**, 22–30.
12 N. Semagina, M. Grasemann, N. Xanthopoulos, A. Renken and L. Kiwiminsker, *J. Catal.*, 2007, **251**, 213–222.
13 L. Shen, S. Mao, J. Li, M. Li, P. Chen, H. Li, Z. Chen and Y. Wang, *J. Catal.*, 2017, **350**, 13–20.
14 C. Berguerand, I. Yuranov, F. Cárdenas-Lizana, T. Yuranova and L. Kiwi-Minsker, *J. Phys. Chem. C*, 2014, **118**, 12250–12259.
15 L. B. Okhlopkova, E. V. Matus, I. P. Prosvirin, M. A. Kerzhentsev and Z. R. Ismagilov, *J. Nanopart. Res.*, 2015, **17**, 475.
16 L. Okhlopkova, I. Prosvirin, M. Kerzhentsev and Z. Ismagilov, *Catalysts*, 2022, **12**, 1660.
17 J. Shi, K. Dou, D. Xie and F. Zhang, *Appl. Catal. O: Open*, 2024, **191**, 206917.
18 S. Mao, B. Zhao, Z. Wang, Y. Gong, G. Lü, X. Ma, L. Yu and Y. Wang, *Green Chem.*, 2019, **21**, 4143–4151.
19 S. K. Johnston, N. Cherkasov, E. Pérez-Barrado, A. Aho, D. Y. Murzin, A. O. Ibhadon and M. G. Francesconi, *Appl. Catal., A*, 2017, **544**, 40–45.
20 J. M. Nadgeri, M. M. Telkar and C. V. Rode, *Catal. Commun.*, 2008, **9**, 441–446.
21 M. Crespo-Quesada, A. Yarulin, M. Jin, Y. Xia and L. Kiwi-Minsker, *J. Am. Chem. Soc.*, 2011, **133**, 12787–12794.
22 **https://pmm.umicore.com/en/prices/palladium/**, (accessed 8 July 2025).
23 **https://markets.businessinsider.com/commodities/nickel-price/euro**, (accessed 8 July 2025).
24 F. Studt, F. Abild-Pedersen, T. Bligaard, R. Z. Sørensen, C. H. Christensen and J. K. Nørskov, *Science*, 2008, **320**, 1320–1322.
25 S. Tanielyan, S. Schmidt, N. Marin, G. Alvez and R. Augustine, *Top. Catal.*, 2010, **53**, 1145–1149.
26 X. Chen and C. Liang, *Catal. Sci. Technol.*, 2019, **9**, 4785–4820.
27 F. M. Bautista, J. M. Campelo, A. Garcia, R. Guardeño, D. Luna and J. M. Marinas, in *Studies in Surface Science and Catalysis*, Elsevier, 1991, vol. 59, pp. 269–276.
28 H. Wu, L. Guo, F. Ma, Y. Wang, W. Mo, X. Fan, H. Li, Y. Yu, I. Mian and N. Tsubaki, *Catal. Sci. Technol.*, 2019, **9**, 6598–6605.
29 C. Wang, Y. Tian, R. Wu, H. Li, B. Yao, Y. Zhao and T. Xiao, *ChemCatChem*, 2019, **11**, 4777–4787.
30 D. Albani, K. Karajovic, B. Tata, Q. Li, S. Mitchell, N. López and J. Pérez-Ramírez, *ChemCatChem*, 2019, **11**, 457–464.
31 Y. Liu, J. Zhao, J. Feng, Y. He, Y. Du and D. Li, *J. Catal.*, 2018, **359**, 251–260.
32 G. Totarella and P. E. De Jongh, *ChemCatChem*, 2024, **16**, e202400334.
33 A. A. Shesterkina, A. A. Strekalova, E. V. Shuvalova, G. I. Kapustin, O. P. Tkachenko and L. M. Kustov, *Catalysts*, 2021, **11**, 625.
34 A. S. Rajpurohit, V. R. M. Talla, M. Jaccob, K. K. Ramaswamy and B. Viswanathan, *Sustainable Energy Fuels*, 2023, **7**, 2861–2872.
35 P. Sudarsanam, H. Li and T. V. Sagar, *ACS Catal.*, 2020, **10**, 9555–9584.
36 R. Balaga, K. Ramineni, X. Zhang, P. Yan, M. R. Marri, V. Perupogu and Z. C. Zhang, *Catalysts*, 2022, **12**, 1286.
37 K. J. A. Raj, M. G. Prakash, R. Mahalakshmy, T. Elangovan and B. Viswanathan, *Chin. J. Catal.*, 2012, **33**, 1299–1305.
38 R. A. Spurr and H. Myers, *Anal. Chem.*, 1957, **29**, 760–762.
39 A. J. Patil, M. H. Shinde, H. S. Potdar, S. B. Deshpande, S. R. Sainkar, S. Mayadevi and S. K. Date, *Mater. Chem. Phys.*, 2001, **68**, 7–16.
40 S. M. Hassan, A. I. Ahmed and M. A. Mannaa, *Ceram. Int.*, 2018, **44**, 6201–6211.
41 J. Tian, H. Gao, H. Deng, L. Sun, H. Kong, P. Yang and J. Chu, *J. Alloys Compd.*, 2013, **581**, 318–323.
42 C. Castañeda, F. Tzompantzi, A. Rodríguez-Rodríguez, M. Sánchez-Dominguez and R. Gómez, *J. Chem. Technol. Biotechnol.*, 2018, **93**, 1113–1120.
43 P. Li, S. Zhang, Z. Xiao, H. Zhang, F. Ye, J. Gu, J. Wang, G. Li and D. Wang, *Fuel*, 2024, **357**, 129817.
44 T. Sreethawong, S. Ngamsinlapasathian and S. Yoshikawa, *Chem. Eng. J.*, 2012, **192**, 292–300.

45 D. Wu, S. Liu, Y. Nie, D. Sun, Y. Zhou, S. Yang, C. Xu, T. Ma and H. Zhang, *Chem. Eng. J.*, 2025, **518**, 164511.
46 X. Zhang, P. Yan, B. Zhao and Z. C. Zhang, *Catal. Sci. Technol.*, 2021, **11**, 297–311.
47 M. A. Nieva, M. M. Villaverde, A. Monzón, T. F. Garetto and A. J. Marchi, *Chem. Eng. J.*, 2014, **235**, 158–166.
48 H. E. Kissinger, *J. Res. Natl. Bur. Stand.*, 1956, **57**, 217.
49 Q. Jeangros, T. W. Hansen, J. B. Wagner, C. D. Damsgaard, R. E. Dunin-Borkowski, C. Hébert, J. Van Herle and A. Hessler-Wyser, *J. Mater. Sci.*, 2013, **48**, 2893–2907.
50 J. Richardson, *Appl. Catal., A*, 2003, **246**, 137–150.
51 K. H. Tonge, *Thermochim. Acta*, 1984, **74**, 151–166.
52 A. Gervasini, *J. Catal.*, 1991, **131**, 190–198.
53 A. P. Grosvenor, M. C. Biesinger, R. St. C. Smart and N. S. McIntyre, *Surf. Sci.*, 2006, **600**, 1771–1779.
54 J. K. Kim, *Polymers*, 2019, **11**, 120.
55 B. Cui, H. Wang, J. Han, Q. Ge and X. Zhu, *J. Catal.*, 2022, **413**, 880–890.
56 J. L. Rodríguez, T. Poznyak, M. A. Valenzuela, H. Tiznado and I. Chairez, *Chem. Eng. J.*, 2013, **222**, 426–434.
57 M. Senna, V. Šepelák, J. Shi, B. Bauer, A. Feldhoff, V. Laporte and K.-D. Becker, *J. Solid State Chem.*, 2012, **187**, 51–57.
58 S. Vernuccio, P. R. Von Rohr and J. Medlock, *Ind. Eng. Chem. Res.*, 2015, **54**, 11543–11551.
59 P. Weerachawanasak, O. Mekasuwandumrong, M. Arai, S.-I. Fujita, P. Praserthdam and J. Panpranot, *J. Catal.*, 2009, **262**, 199–205.
60 J. P. Boitiaux, J. Cosyns and E. Robert, *Appl. Catal.*, 1987, **32**, 145–168.
61 Á. Molnár, A. Sárkány and M. Varga, *J. Mol. Catal. A: Chem.*, 2001, **173**, 185–221.
62 J. Carrasco, G. Vilé, D. Fernández-Torre, R. Pérez, J. Pérez-Ramírez and M. V. Ganduglia-Pirovano, *J. Phys. Chem. C*, 2014, **118**, 5352–5360.
63 S. Katheria, A. Gupta, G. Deo and D. Kunzru, *Int. J. Hydrogen Energy*, 2016, **41**, 14123–14132.